

## Supporting Information

### **Fe<sup>3+</sup>-Bridged Cellulose–Alginate Composite Gel Beads as Stable and Effective Photo-Fenton Catalysts**

Wen Wang, Songlin Fan, Yanjuan Zhang\*, Chao Fan, Zuqiang Huang\*, Huayu Hu, and Yuben Qin

School of Chemistry and Chemical Engineering, Guangxi University, Nanning 530004, China

\*Corresponding authors. Tel.: +86-771-3233718; Fax: +86-771-3233718.

E-mail addresses: zhangyj@gxu.edu.cn (Y. Zhang), huangzq@gxu.edu.cn (Z. Huang).

**2.5. Characterizations.** The microstructures of the samples were observed by scanning electron microscopy (SEM, S-3400N, Hitachi, Japan) at a voltage of 5 kV and energy-dispersive X-ray spectroscopy (EDS) (Hitachi, Japan). X-ray diffractometry (XRD) crystal structure analysis of the samples was carried out using a D/MAX2500 V X-ray diffractometer (Rigaku, Japan) using Cu- $K_\alpha$  radiation ( $\lambda = 0.154$  nm) generated at 40 kV and 30 mA. The XRD patterns were obtained between  $2\theta$  values of  $5^\circ$  to  $80^\circ$ . The crystallinity of cellulose was calculated using Eq. (1) <sup>1</sup>:

$$CrI = \frac{I_{002} - I_{am}}{I_{002}} \times 100\% \quad (1)$$

Where  $CrI$  is the crystallinity index,  $I_{002}$  is the maximum diffraction intensity of the (002) reflection, and  $I_{am}$  is the diffraction intensity at  $2\theta = 18^\circ$ .

Fourier transform infrared spectroscopy (FTIR) spectra were recorded using an FTIR-8400S spectrometer (Shimadzu, Kyoto, Japan) between 400 and 4000  $\text{cm}^{-1}$ . X-ray photoelectron spectroscopy (XPS) was performed using an ESCALAB 250Xi XPS (Thermo Fisher Scientific, USA) with Al- $K_\alpha$  radiation (1486.6 eV). The specific surface area and pore size distributions of the dry samples were measured by the multilayer  $\text{N}_2$  adsorption method using a Gemini VII 2390 automatic rapid surface area analyzer (Micromeritics, USA) and were calculated using the Brunauer–Emmett–Teller (BET) method and Barrett–Joyner–Halenda (BJH) model, respectively. The compressive strengths of different samples were measured using an Instron DNS-100 universal testing machine (Changchun Testing Machine Research Institute, China). The Ca and Fe contents in the gel beads were determined using inductively coupled plasma atomic emission spectroscopy (ICP-AES, 720ES, Agilent, USA). The point of zero charge

( $\text{pH}_{\text{PZC}}$ ) of the samples was measured by potentiometric titration. The absorption of the samples in the UV-vis light range was measured using a Lambda 1050<sup>+</sup> UV-vis spectrometer (PerkinElmer, USA) with  $\text{BaSO}_4$  as a reference, and the band gaps ( $E_g$ ) of all samples were calculated using the Tauc plot method. The rate of electron–hole generation/recombination was evaluated by photoluminescence (PL) spectroscopy using an FLS100 fluorescence spectrophotometer (Edinburgh, UK) at an excitation wavelength of 325 nm. Electrochemical impedance spectroscopy (EIS) was performed using an electrochemical system (CHI 760E, China), and EIS experiments were conducted on an electrochemical workstation at room temperature (Princeton Applied Research 4000+) with the prepared electrodes in 0.1 M KCl solution containing 5 mM  $\text{K}_3[\text{Fe}(\text{CN})_6]/\text{K}_4[\text{Fe}(\text{CN})_6]$  (1:1). The frequency range was 0.01–100 kHz. Infrared thermal imaging analysis was achieved using an analog daylight lamp source (PLS-SXE300C), which yielded an intensity of 100 mW/cm<sup>2</sup>, as measured by an FZ-A radiometer. Infrared photos were captured using an infrared camera (CHAUVIN ARNOUX/CA73). A non-contact infrared thermometer (GM320, Benetech) was used to measure the temperature. Electron spin resonance (ESR) analysis was conducted using an A300-10/12 electron paramagnetic resonance spectrometer (Bruker AXS Company, Germany). The MB degradation intermediates were determined using liquid chromatography coupled with mass spectrometry (UPLC-MS, Thermo Scientific, USA).

**3.1. Sample Characterization.** The changes in the functional groups of the cellulose before and after the different pretreatments were determined using FTIR analysis (Figure S1a). The FTIR spectra of MAC and MAFCC showed no new absorption peaks compared with that of the original cellulose, indicating that pretreatment did not induce the formation of new functional groups. However, the characteristic absorption peaks shifted. Specifically, the absorption peak corresponding to hydroxyl groups was observed at  $3423\text{ cm}^{-1}$  in the spectrum of the original cellulose, but, in the spectra of MAC and MAFCC, this peak broadened and shifted to  $3434$  and  $3432\text{ cm}^{-1}$ , respectively. The shift in this peak for MAFCC is smaller than that of MAC, and this is a result of the interactions between  $\text{FeCl}_3$  and the hydroxyl groups of cellulose,<sup>2</sup> suggesting that the hydrogen bonding in the cellulose was weakened, potentially increasing its accessibility and reactivity.

The crystal structures of the different samples were characterized using XRD measurements (Figure S1c). The peaks at  $2\theta = 15.1^\circ$ ,  $16.2^\circ$ , and  $22.4^\circ$  were assigned to the (1-10), (110), and (200) planes of crystalline cellulose I, respectively.<sup>3</sup> Compared with that of untreated cellulose (80.37%), the crystallinities of MAC and MAFCC decreased to 42.03% and 30.03%, respectively. The more significant decrease in crystallinity for MAFCC further indicates that the  $\text{FeCl}_3$  promoted the destruction of the crystal structure of cellulose on the application of mechanical activation.

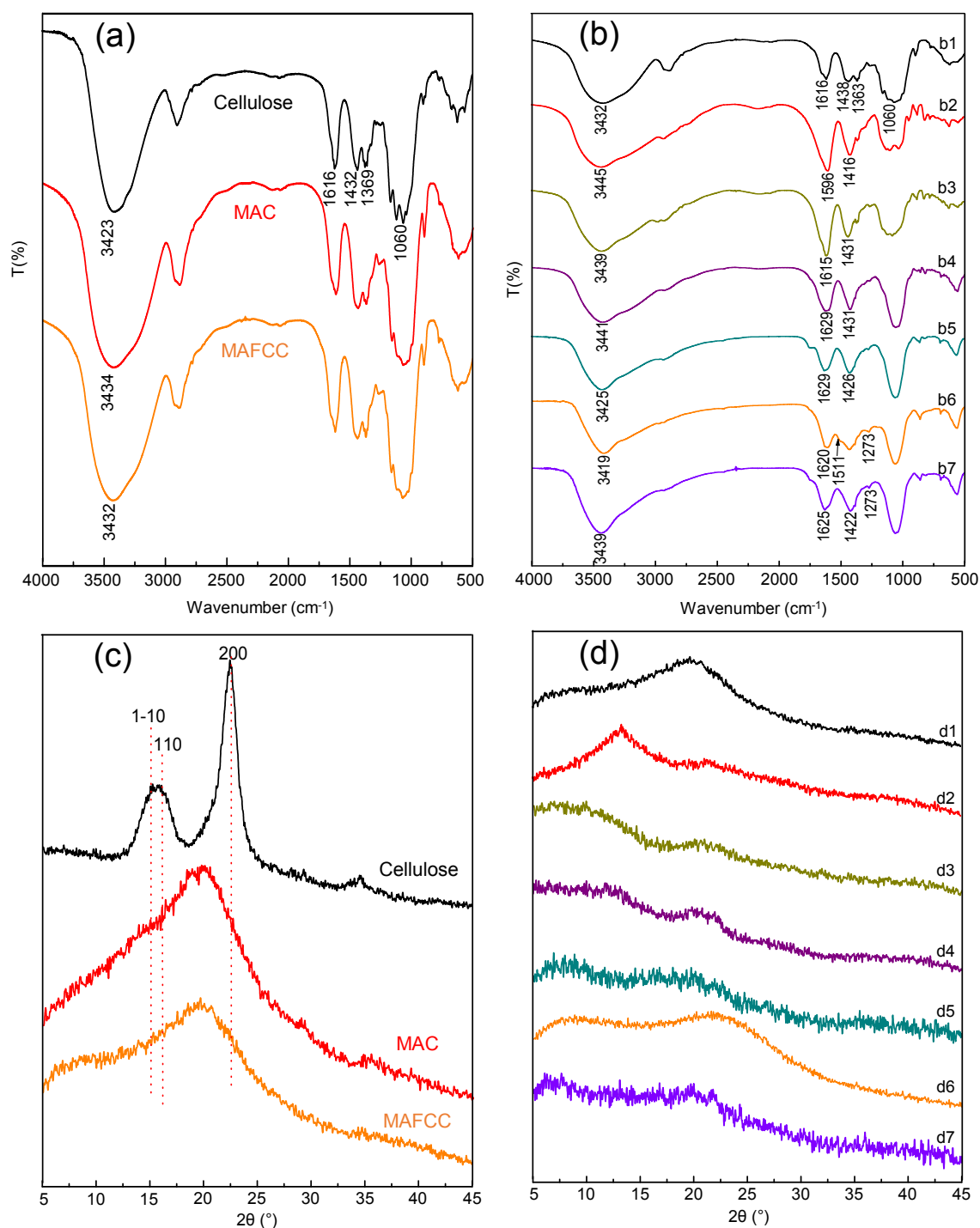


**Figure S1.** (a) FTIR spectra of cellulose, MAC, and MAFCC; (b) FTIR spectra of (b1) MAFCC, (b2) NaAlg, (b3) MAC-Alg/Ca, (b4) MAFCC-Alg/Ca, (b5) MAFCC-Alg/Ca-Fe, (b6) PDA, and (b7) MAFCC-Alg/Ca-Fe@PDA; (c) XRD patterns of cellulose, MAC, and MAFCC; (d) XRD patterns of (d1) MAFCC, (d2) NaAlg, (d3) MAC-Alg/Ca, (d4) MAFCC-Alg/Ca, (d5) MAFCC-Alg/Ca-Fe, (d6) PDA, and (d7) MAFCC-Alg/Ca-Fe@PDA.

The changes in the morphology of cellulose before and after different treatments were observed by SEM ([Figure S2](#)). The untreated cellulose was observed to have the form of long fibers, and their surfaces were relatively complete and smooth. After MA and MAFC treatment, the long fiber structure disappeared, and small block-like particles were observed. However, the MAFCC showed more uniform damage to the cellulose, and the particles were smaller than those of MAC, indicating that MAFC pretreatment destroyed the long fiber structure of cellulose to a greater extent, which is favorable for increasing the activity and solubility of cellulose.

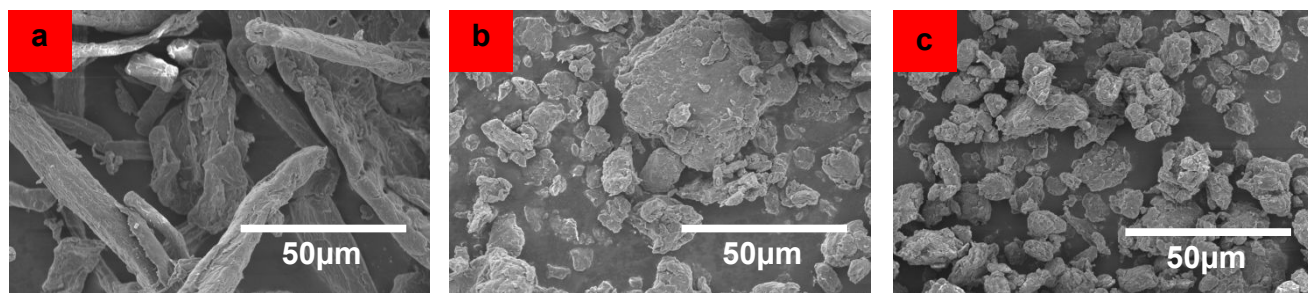


**Figure S2.** SEM images of (a) untreated cellulose, (b) MAC, and (c) MAFCC.

After PDA modification, the surface structure of the gel beads was rough and wrinkled, nanoscale spherical particles were present, and the interior was observed to have an irregular porous network structure with a dense and stable structure (Figure S3b). An SEM image of a cross-section of a MAFCC-Alg/Ca-Fe@PDA bead is shown in Figure S3a. The thickness of the PDA coating is about 5  $\mu\text{m}$ , and energy dispersive X-ray analysis confirmed the inherent N components of PDA, as shown in Figure S3c. The N content was mainly concentrated in the PDA coating on the surface of the gel bead, although a small amount was present close to the surface of the gel bead. Thus, the PDA layer was uniformly coated on the surface of the gel beads through covalent and noncovalent interactions between PDA and MAFCC-Alg/Ca-Fe.

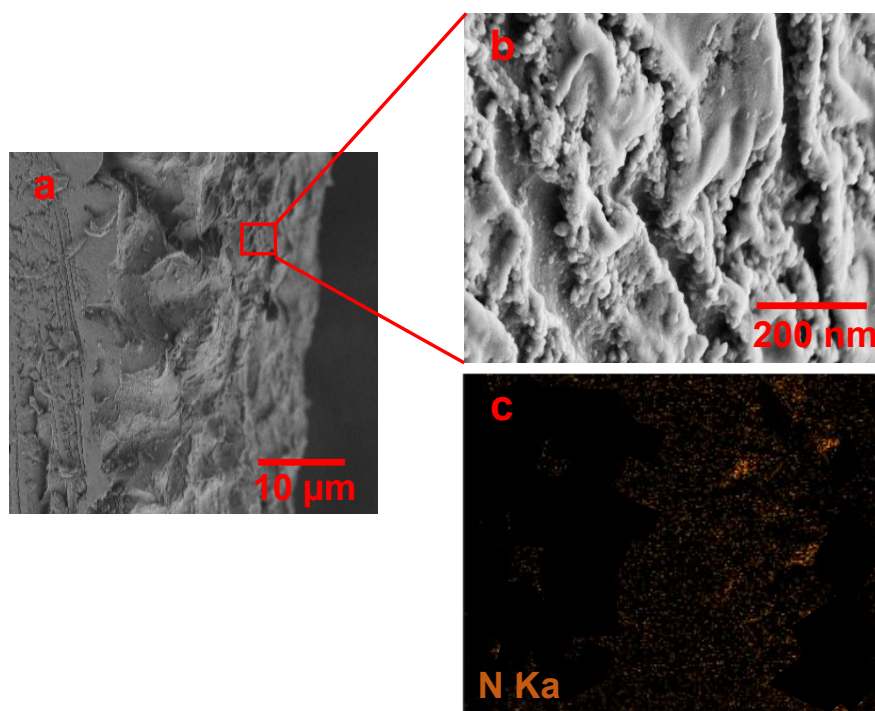


**Figure S3.** SEM images of (a) the cross-section of MAFCC-Alg/Ca-Fe@PDA, (b) the external magnified image of MAFCC-Alg/Ca-Fe@PDA, and (c) the N element analysis by SEM-EDS.

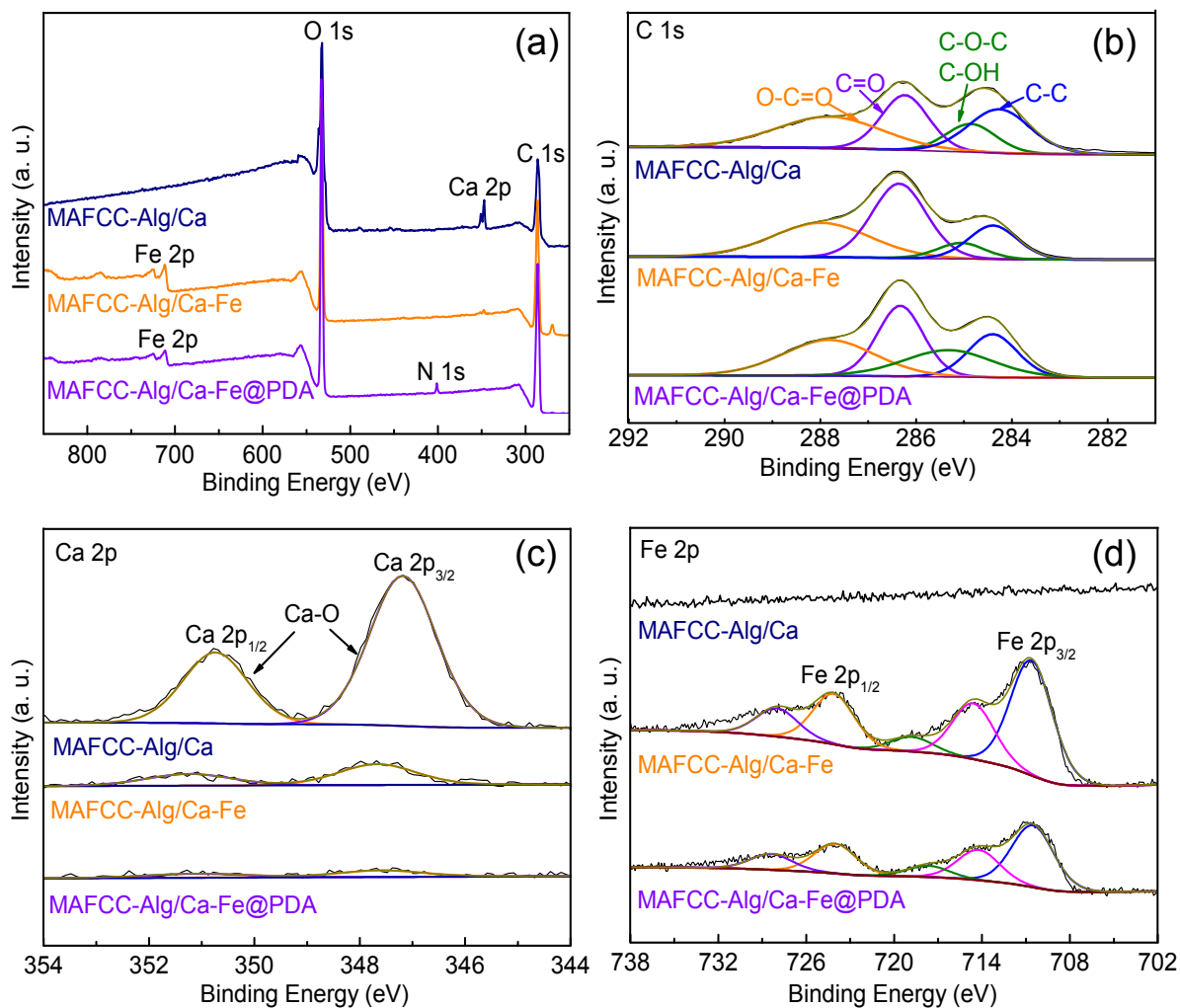


**Figure S4.** XPS spectra of different samples: (a) full-survey spectra, (b) C 1s peak fitting curves, (c) Ca 2p peak fitting curves, and (d) Fe 2p peak fitting curves.



**Table S1** Specific surface areas, pore volumes, mean pore sizes, and compressive strengths of different samples.

Sample	Specific surface area (m <sup>2</sup> g <sup>-1</sup> )	Pore volume (cm <sup>3</sup> g <sup>-1</sup> )	Mean pore size (nm)	Compressive strength (MPa)
FeAlg	68.98	0.13	14.25	0.22
CaAlg	26.68	0.064	17.61	0.28
Alg/Ca-Fe	96.87	0.45	10.48	0.23
MAC-Alg/Ca-Fe	108.74	0.31	16.53	0.76
(MAC+Fe)-Alg/Ca-Fe	128.17	0.33	10.88	0.78
MAFCC-Alg/Ca-Fe	138.99	0.24	11.15	0.92
MAFCC-Alg/Ca-Fe@PDA	153.44	0.51	16.81	1.24

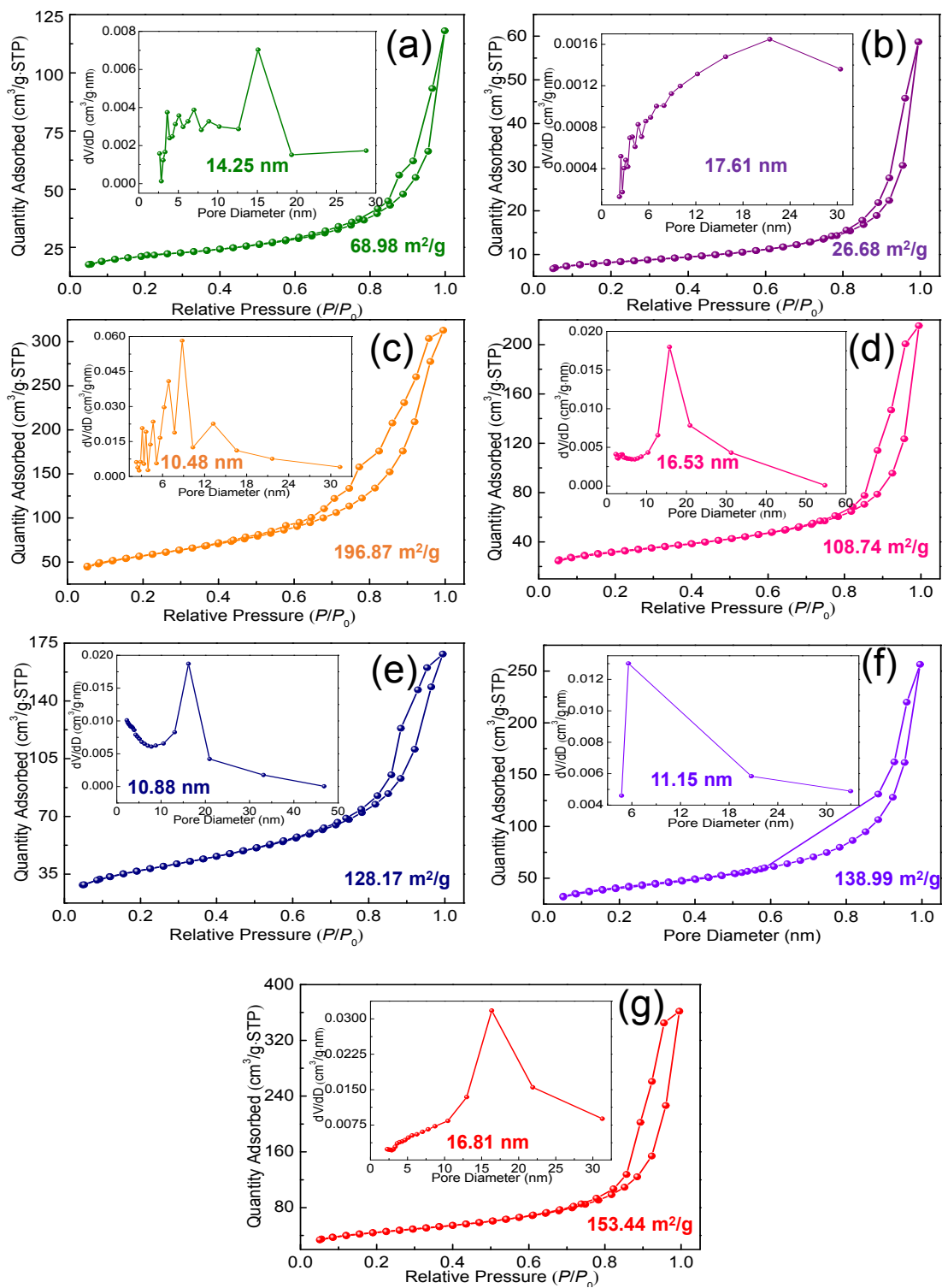


**Figure S5.** N<sub>2</sub> adsorption–desorption isotherms and pore distributions of different samples: (a) FeAlg, (b) CaAlg, (c) Alg/Ca-Fe, (d) MAC-Alg/Ca-Fe, (e) (MAC+Fe)-Alg/Ca-Fe, (f) MAFCC-Alg/Ca-Fe, and (g) MAFCC-Alg/Ca-Fe@PDA.

The structural stability of the gel beads was tested by examining the morphology of the MAFCC-Alg/Ca-Fe@PDA and FeAlg gel beads before and after mechanical extrusion under the same load (Figure S6). The gel beads are easily compressed under pressure, and their shape is not easily recovered when the load is removed. In particular, the FeAlg beads broke into fragments when subjected to external pressure. However, the MAFCC-Alg/Ca-Fe@PDA gel beads remained compact, even after compression into flat discs. This result suggests that the MAFCC-Alg/Ca-Fe@PDA gel beads had high structural stability, which is consistent with the compressive strength results. This increased structural stability suggests that the modification with MAFCC and PDA reduces the risk of secondary pollution caused by physical damage, and this is of great significance concerning the use of gel beads as catalysts with practical engineering applications. In addition, the stability of the beads could have a significant effect on their photocatalytic activity.

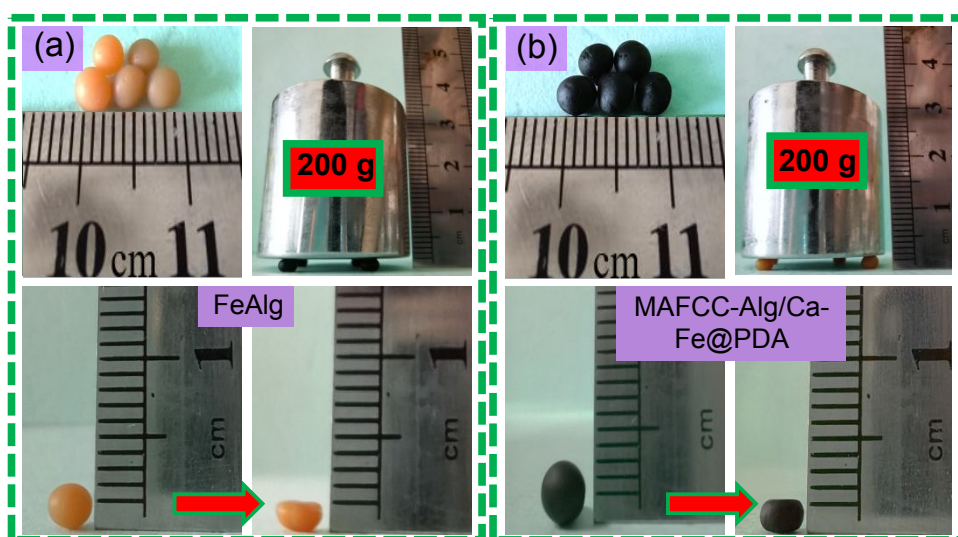
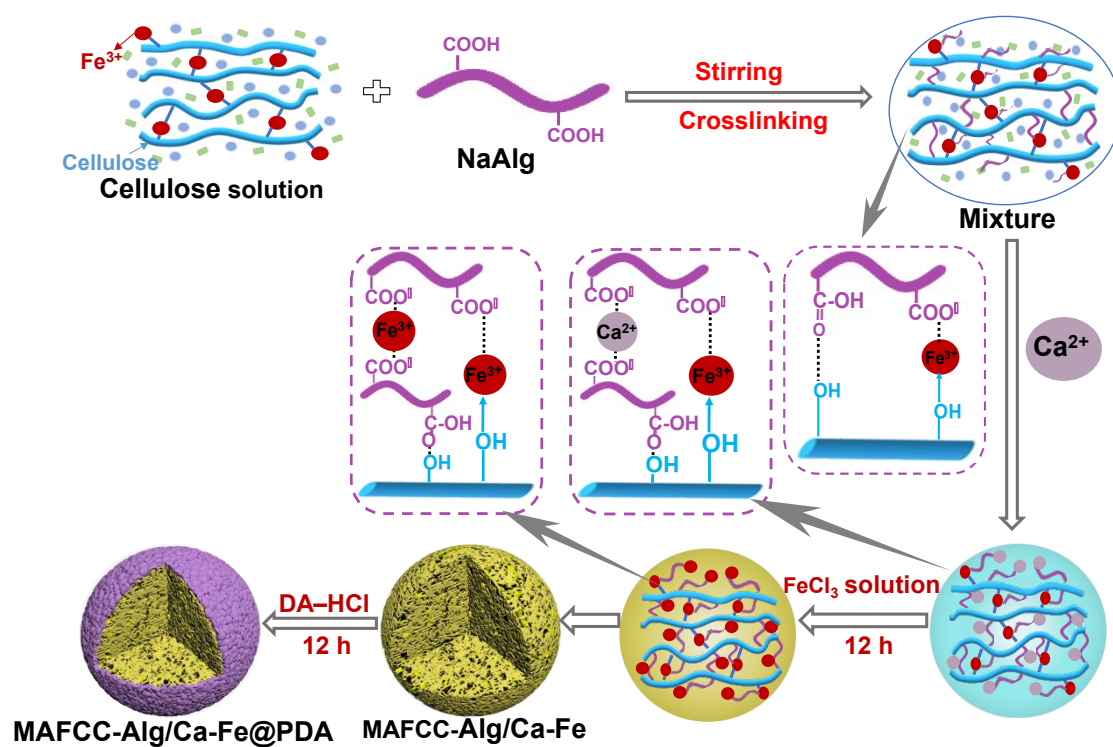


**Figure S6.** The appearance changes of (a) FeAlg and (b) MAFCC-Alg/Ca-Fe@PDA under the same load.

**Table S2** Effect of  $\text{FeCl}_3$  concentration on the iron and calcium content of MAFCC-Alg/Ca-Fe.

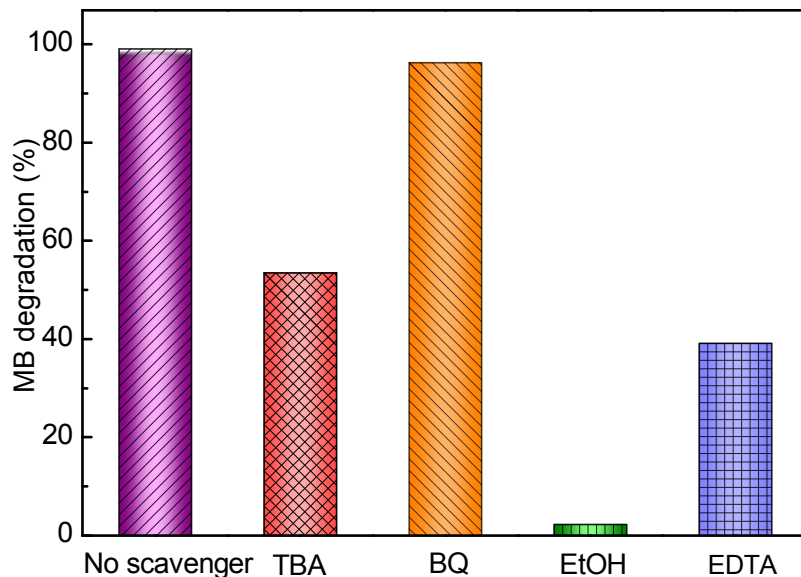
MAFCC-Alg/Ca-Fe	FeCl <sub>3</sub> concentration (M)						
	0	0.05	0.1	0.3	0.5	0.7	0.9
Calcium content (%)	16.35	0.30	0.24	0.16	0.084	0.049	0.034
Iron content (%)	0.14	9.31	10.25	11.69	11.76	12.24	12.22

Experimental conditions:  $\text{CaCl}_2$  concentration = 5 wt%; loading time = 12 h.

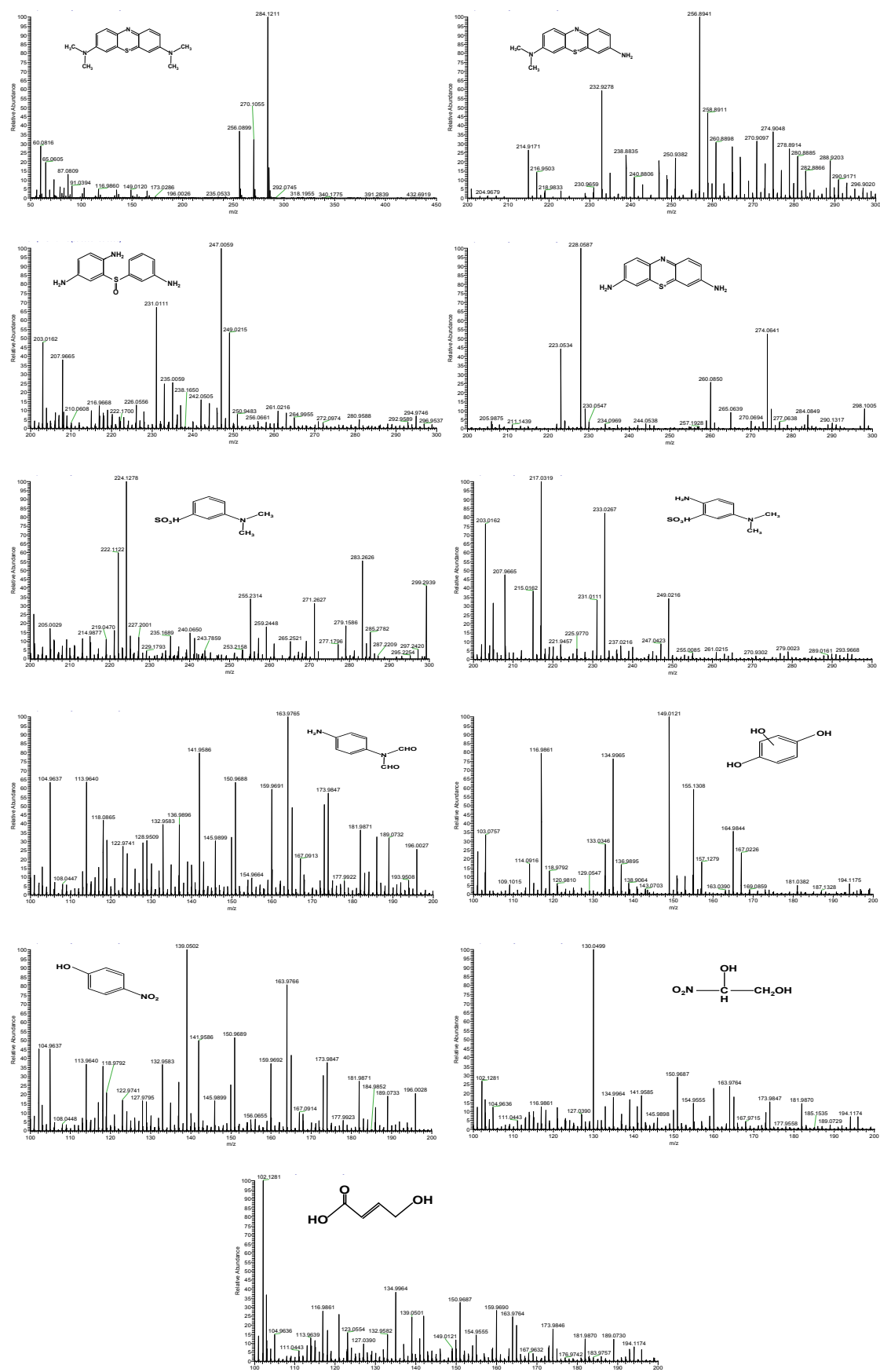


**Figure S7.** Schematic diagram of the synthesis process of MAFCC-Alg/Ca-Fe@PDA.

**3.4. Proposed Photo-Fenton Rreaction Mechanism.** The quenching experiments were carried out to verify the active species involved in the photo-Fenton process further. As shown in Figure S8, the degradation of MB decreased slightly after the addition of tertiary butyl alcohol (TBA, a  $\cdot\text{OH}$  scavenger) and EDTA (a hole scavenger) into the reaction system, indicating that  $\cdot\text{OH}$  and holes have roles in the catalytic degradation reaction. After the addition of ethanol (an electron scavenger), the degradation of MB was significantly reduced, whereas the introduction of 1,4-benzoquinone (BQ, a  $\cdot\text{O}_2^-$  scavenger) had almost no effect on the degradation of MB, suggesting that  $\cdot\text{O}_2^-$  is not a key species in this system. In summary,  $\cdot\text{OH}$  electrons and holes are the main active species involved in MB degradation in our photo-Fenton MAFCC-Alg/Ca-Fe@PDA system.

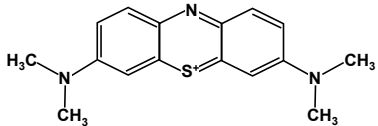
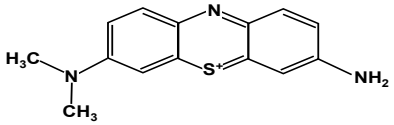
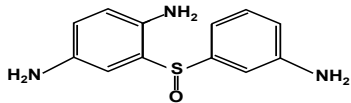
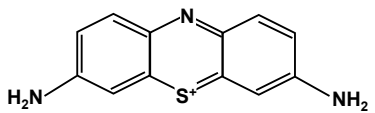
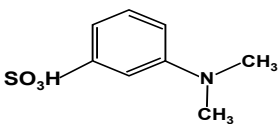
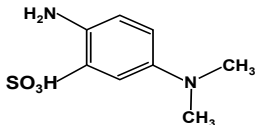
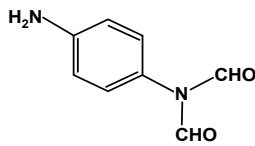
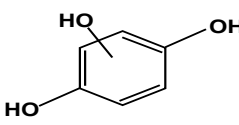
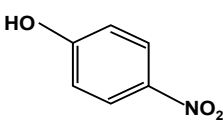
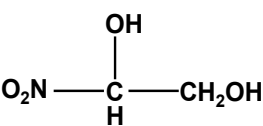
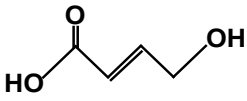


**Figure S8.** Effect of radical scavengers on MB degradation. TBA: *tert*-Butyl amine; BQ: benzoquinone; EDTA: ethylenediaminetetraacetic acid. Reaction conditions:  $C_0$  (MB) = 50 mg L<sup>-1</sup>, [H<sub>2</sub>O<sub>2</sub>] = 18 mM, [catalyst] = 1 g L<sup>-1</sup>, temperature = 25 °C, and pH = 5.



**Figure S9.** LC-MS molecular mass profiles of intermediates.

**Table S3** Main intermediates from the degradation of MB determined by LC-MS.

	Molecular formula	m/z	Structural formula
1	$C_{16}H_{18}N_3S$	284	
2	$C_{14}H_{14}N_3S$	256	
3	$C_{12}H_{10}N_3S$	228	
4	$C_{12}H_{13}N_3SO$	247	
5	$C_8H_{11}NSO_3Na$	224	
6	$C_8H_8N_2O_2$	164	
7	$C_8H_{12}N_2SO_3$	217	
8	$C_6H_6O_3Na$	149	
9	$C_6H_5O_3N$	139	
10	$C_2H_5NO_4Na$	130	
11	$C_4H_6O_3$	102	



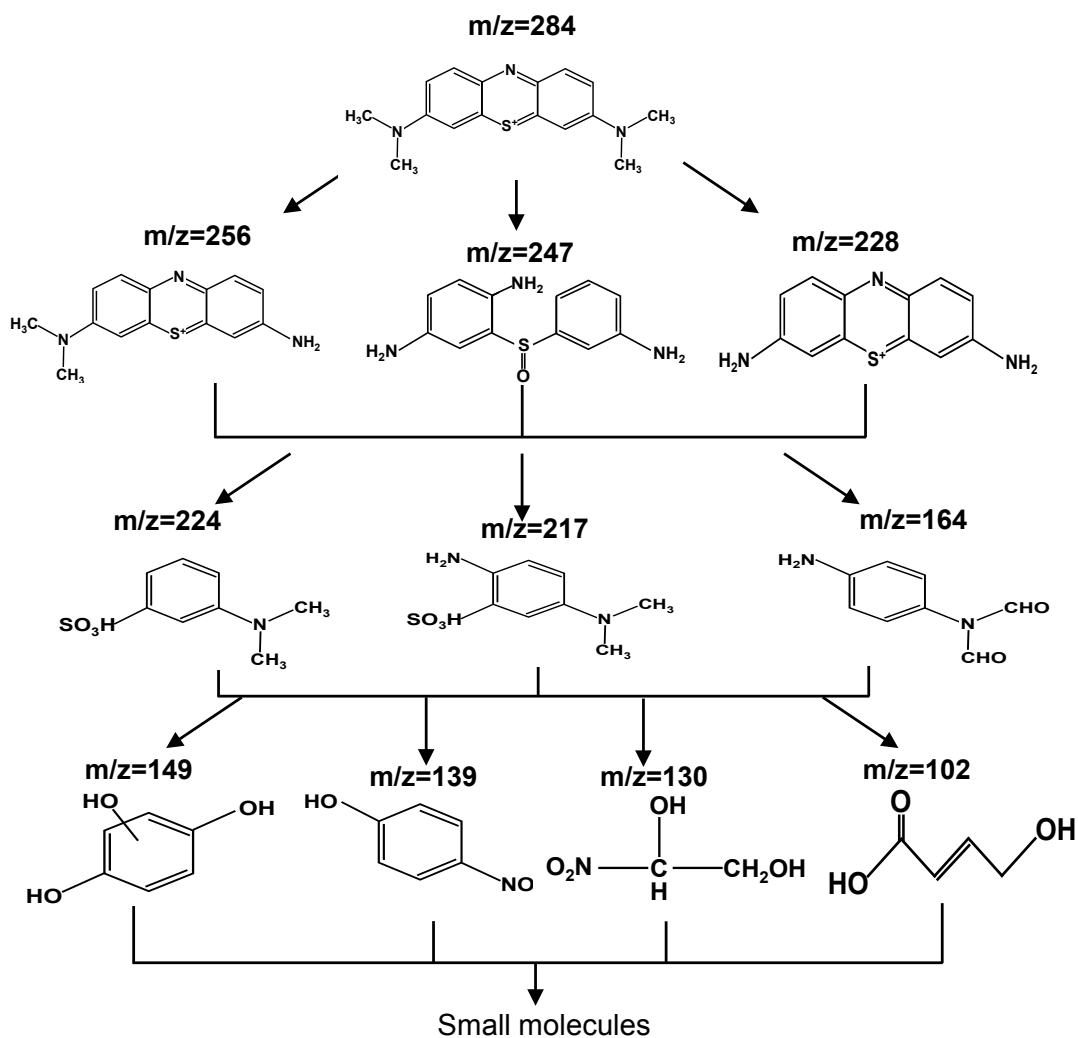


**Figure S10.** Proposed degradation pathway of MB in photo-Fenton process.

## REFERENCES

- (1) Kim, S.; Holtzapple, M. T. Effect of structural features on enzyme digestibility of corn stover. *Bioresour. Technol.* **2006**, *97*, 583–591.
- (2) Zhang, H.; Lyu, G.; Zhang, A.; Li, X.; Xie, J. Effects of ferric chloride pretreatment and surfactants on the sugar production from sugarcane bagasse. *Bioresour. Technol.* **2018**, *265*, 93.
- (3) Zhang, Y.; Li, Q.; Su, J.; Lin, Y.; Huang, Z.; Lu, Y.; Sun, G.; Yang, M.; Huang, A.; Hu, H.; Zhu, Y. A green and efficient technology for the degradation of cellulosic materials: Structure changes and enhanced enzymatic hydrolysis of natural cellulose pretreated by synergistic interaction of mechanical activation and metal salt. *Bioresour. Technol.* **2015**, *177*, 176–181.